Fachtagung "Lasermethoden in der Strömungsmesstechnik"

3. – 5. September 2013, München

Application of Tomographic PIV on a Passage Vortex in a Transonic Compressor Cascade

Anwendung von Tomografischem PIV zur Messung des Passagenwirbels in einem transsonischen Verdichter Gitter

Joachim Klinner, Melanie Voges, Christian Willert
Institut für Antriebstechnik, Deutsches Zentrum für Luft- und Raumfahrt, Linder Höhe, 51147 Köln

Transsonischer Gitterwindkanal, tomografisches PIV, Lichtschnittsonde, MENT
transonic cascade wind tunnel, tomographic PIV, light sheet probe, MENT

Abstract

The contribution describes the implementation of thick sheet tomographic PIV [Elsinga et al. 2006] in a transonic cascade wind tunnel in order to measure the three dimensional turbulent corner flow in a highly loaded compressor cascade at Ma_1 = 0.6. Under these operation conditions the secondary flow structures in the cascade are dominated by a passage vortex located at the base of the blade and near the suction side. The report describes various aspects of the adaption of the tomographic PIV setup to the restricted access on the cascade wind tunnel. A four camera setup is used to resolve a measuring volume of 36×24×4 mm from which a total of 54×74×13 vectors at a spacing of 0.64 mm in *x* (chord-wise direction) and a spacing of 0.32 mm in *y* and *z* could be recovered. Three dimensional reconstruction of the imaged particle volume is achieved with the maximum entropy reconstruction technique (MENT, [Minerbo, 1978; Bilsky et al., 2012]). The reconstruction quality of experimental data is documented by plots of the reconstructed intensity along volume depth. The extraction of three-dimensional displacement field relies on multi-resolution, 3-D correlation processing with iterative volume deformation. The recovered three-dimensional velocity fields are compared at selected planes with (thin-sheet) stereo PIV data.

Introduction

Thick sheet tomographic PIV (tomo-PIV) and conventional stereo PIV (SPIV) are utilized in order to characterize the three dimensional turbulent corner flow within a highly loaded compressor cascade at Ma_1 =0:60. The oil-streak image shown in Fig. 1 taken from [Hergt et al., 2013] provides an impression of the complex transonic flow pattern at the intersection between endwall and the blade's suction side. The flow is dominated by a passage vortex which is driven by the pitch-wise pressure gradient between pressure and suction side. The time-averaged location of the vortex can also be predicted by a RANS (Reynolds averaged Navier Stokes) simulation as shown in Fig. 2. The vortex and the reverse pressure gradient along the cascade passage cause a flow separation between the endwall and the blade. The corner separation leads to blockage effects which limit the mass flow capacity of the cascade. Under the given test conditions the simulations predict an extension of the passage vortex region of approximately 40×24×15 mm.

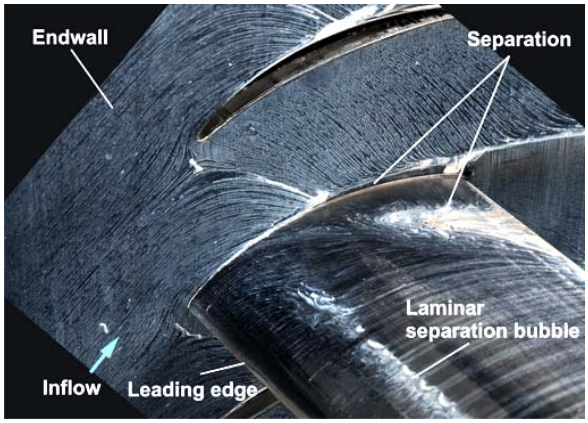

Fig. 1: Oil steak pattern of corner separation [Hergt et al. 2013]

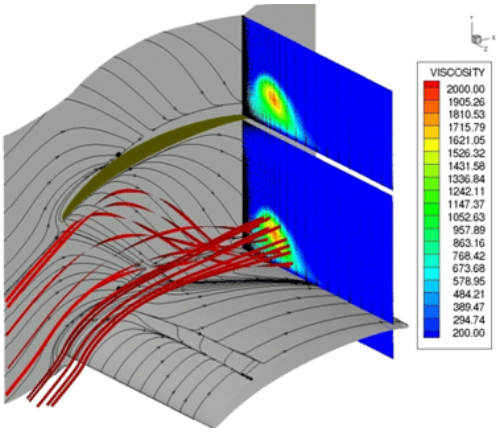

Fig. 2: RANS simulation of corner flow, contour represents eddy viscosity

Table 1: Cascade parameter

Chord length	70 mm
Pitch	40.4 mm
Span width	168 mm
Deflection angle	43°
Ma_1 at aerodynamic design point	0.60
Re based on Chord length	800,000
Free stream turbulence Tu_1	1-4%

Test facility and cascade geometry

The measurements are carried out in the transonic cascade wind tunnel (TGK) of the DLR Institute of Propulsion Technology. The TGK is a closed loop, continuously running facility with a symmetrical nozzle and a variable test section by adjustment of the lower end wall. Additional suction capacities of the system allow the control of the side wall boundary layer in front of the cascade test section, in the upper and lower bypass channels as well as the transonic upper end wall. The suction capacities allow the adjustment of the static pressure across the channel height. Thereby, a homogeneous inflow according to an “infinite blade cascade” is achieved. The cascade consists of seven airfoils that are supported by transparent acrylic side walls of 16 mm thickness which provide suitable optical access for schlieren visualization as well as flow velocity methods such as laser-2-focus velocimetry (L2F) and particle image velocimetry (PIV). Geometry parameters and operation conditions of the cascade are summarized in **Table 1**.

Experimental Implementation of Volumetric and Stereo PIV

Measurements are carried out near the suction side of a single passage in an area coincident with the numerically predicted location of the passage vortex. **Fig. 3** shows a photograph of the tomographic PIV setup which involves four double-frame (PIV) cameras fitted with Scheimpflug mounts to account for the oblique imaging arrangement. The view parameters are summarized in **Table 2**. Two cameras observe the volume of interest along the suction side at zero pitch while the other camera pair observes the measurement volume from above at 26° and 34° pitch in order to have a sufficient angular aperture of the system.

Both single-axis and two-axis Scheimpflug mounts are used to optimize the depth of focus of each camera. The lens apertures range from $f_\#$ 8 to $f_\#$ 16 in order to minimize optical distortions due to the oblique viewing through the acrylic window. The observed common region of interest has a size of approximately 36×24 mm² and is located near the trailing edge of the blade. The thickness of the illuminated volume is successively adjusted to approximately 1

and 3.5 mm at FWHM during each wind tunnel run. Image data is acquired in three regions at distances of 3, 8 and 11 mm from the side wall in order to cover the entire passage vortex. Each volume has a maximum size of 36×24×3.5 mm³ depending on the sheet thickness. Within each region three additional thin sheet stereo PIV (SPIV) measurements are recorded and are later used for comparison (for details on SPIV see [Prasad, 2000, Raffel et al., 2007]).

The light sheet probe (see **Fig. 4** and **Fig. 5**) is introduced 450 mm downstream of the trailing edge of the cascade. The beam enters the cascade through a 500 mm long, 16 mm dia. probe whose tip contains a 90° turning mirror. The probe is additionally supported from the inside of the tunnel in order to reduce aerodynamically induced bending and vibrations which would affect the light sheet position. To improve the protection of the mirror surface from incoming particles (rust) the probe tip was retrofitted with a Laval nozzle which redirects and accelerates the purge flow against the tunnel flow, ideally at supersonic speed [Klinner et al., 2012]. Thereby incoming particles are sufficiently decelerated and prevent the erosion of mirror surface. As illustrated in **Fig. 5** the optical setup of the probe consists of two doublets at the probe entry, the first of which reduces the laser-beam diameter onto inner tube diameter. Together with the cylindrical lens inside the probe the beam is enlarged in one dimension to achieve a height of the sheet of 25 mm in the FOV. The two cylindrical lenses of the second doublet focus the sheet waist at varying distances depending on the spacing between the lenses. This leads to a variable thickness of the sheet within the field of view. With the aid of spacers a reliable and quick variation of sheet thickness can be achieved even during wind tunnel operation.

Table 2: Imaging parameters of tomographic Setup

		Camera 1	Camera 2	Camera 3	Camera 4
Region of interest	[pixel]	1600×1200	1600×1030	1900×1500	2048×1800
Approx. magnification *M*	[-]	0.37	0.31	0.38	0.46
Approx. magnification *M*	[pixel/mm]	50	42	51	62
Focal length	[mm]	100	100	85	100
$f_{\#}$ nominal / effective	[-]	16 / 22	11/ 14	8 / 11	11 / 16
Particle image density at thick sheet	[ppp]	0.018	0.024	0.022	0.015
Particle image diameter	[pixel]	3…5	2…4	2…4	3...4
Yaw / pitch angle		30° / -26°	-15° / -34°	-15° / 0	26° / 0

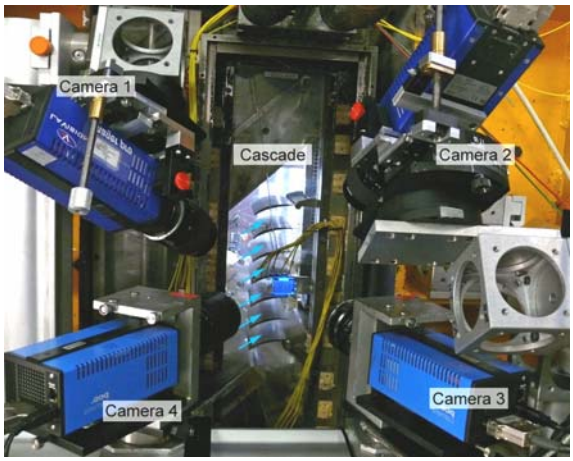

Fig. 3: Tomo PIV setup and back-illuminated calibration target on a micro traverse

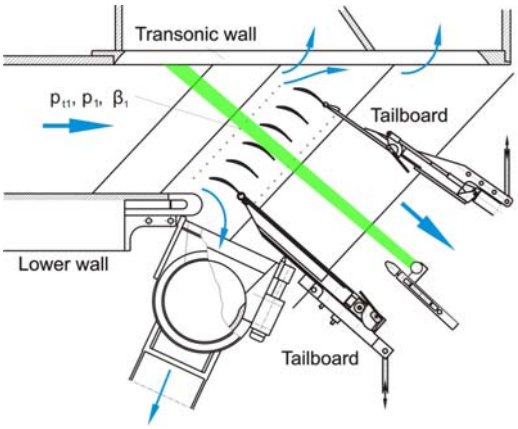

Fig. 4: The TGK test section and light-sheet orientation

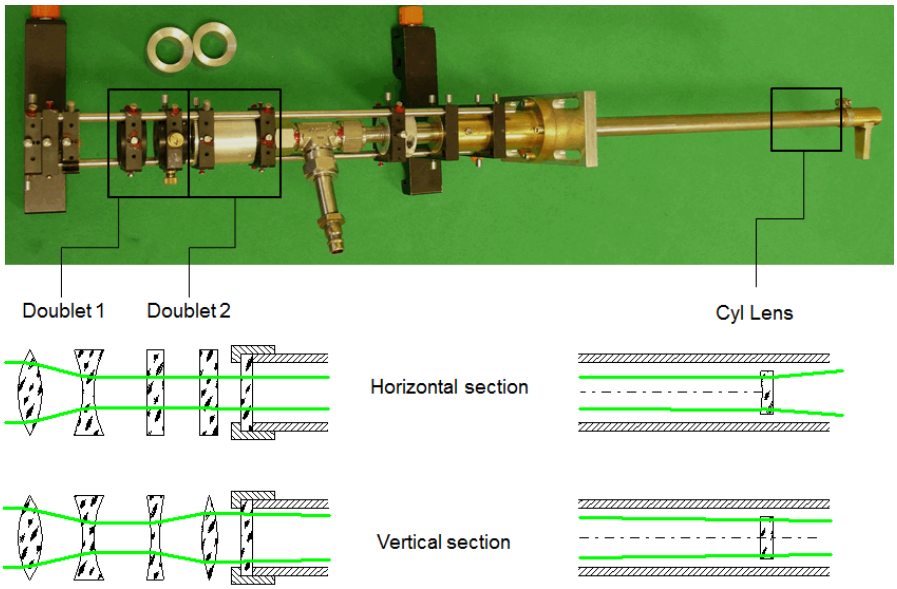

Fig. 5: Optical design of the light-sheet probe

In order to increase the light-sheet thickness in the FOV and at the same time prevent damage to optical components in the probe, the beam waist is shift upstream of the FOV, away from the probe itself. In conjunction with the limited aperture of 6.6×9.4 mm² provided by the Laval nozzle at the probe tip, the maximum achievable sheet thickness is limited to about 5 mm in the probe volume. The maximum light sheet thickness, as measured with a beam profiler, is 3.5 mm FWHM within the FOV at 450 mm distance from the probe tip (see **Fig. 6**). The higher order transverse modes of the flash lamp pumped laser result in a more flat top profile of the thick sheet which therefore strongly deviates from the Gaussian fit. The minimum achievable light sheet thickness is 1.1 mm FWHM at the waist which is used for the stereo PIV reference measurements. The integral pulse energy within the FOV is 50 mJ.

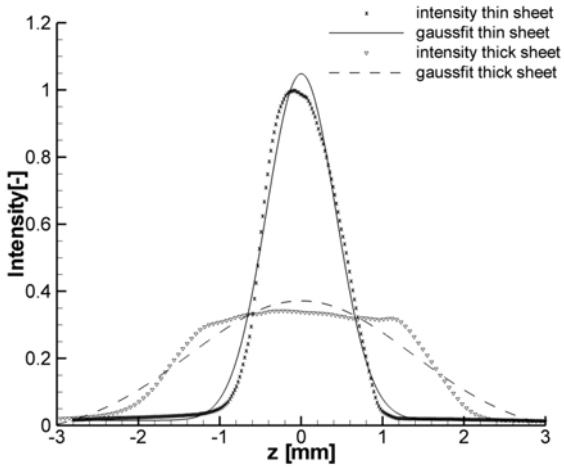

Fig. 6: Light sheet intensity profile vs. volume depth of thick and thin sheet

The cascade wind tunnel facility is seeded with an atomized paraffine-ethanol mixture (1:2) dispersed by two atomizers. An impactor and a dryer between atomizer and test section limited the maximum droplet diameter to approximately 1 µm. In an effort of improving the global seeding homogeneity a seeding injection rake was installed on the screens within the settling chamber upstream of the test section. This ensured the distribution of the particles over a larger area compared to streamline seeding. A response time evaluation of the applied seeding can be found in [Klinner et al., 2012] and reports a shock response time of 0.77±0.15 µs based upon based upon velocity profiles measured across a normal shock at Ma_1=1.25. The

average response length corresponds to 0.23±0.045 mm. Based on Stokes drag law for spherical particles and a particle density of ρ_p=0.85 g/cm³ with the ethanol part fully evaporated and a maximum particle slip velocity of Δu=150 m/s this would lead to an average particle diameter of about d_p=0.4 µm. The achieved particle image densities (see **Table 2**) were evaluated using image segmentation algorithms based on connected component labeling. In the thick sheet configuration the measured particle image density in the separated corner flow ranges between 0.015-0.024 ppp (particle per pixel) depending on the view's magnification. The particle image size varies between 2 and 5 pixel, is partially elliptical and depends on the effective lens aperture and on residual astigmatism effects within each particular view.

Camera calibration and accuracy

The volume is calibrated with a traversed micro target [Klinner & Willert, 2012]. The measured point correspondences of world and camera coordinates are used to fit mapping functions according to world-to-image and image-to-world projection for later reconstruction. The residuals of the least squares minimization of the re-projection error can be found in **Table 3**. Global image shifts due to tunnel vibrations are monitored simultaneously with tomographic measurements. Thus particle image recordings additionally contain images of laser illuminated small reference marks on the Perspex sidewalls. These small marks were correlated with appropriate regions of the average image of the PIV recording. This a posteriori correction is only possible for the measurement volumes at 3 and 8 mm distance from the sidewall, where both marks and particles still are within camera focus. The image shifts due to tunnel vibrations are on the order of ≈0.5 pixel for cameras 3 and 4 and of ≈1 pixel for camera no.1. By comparison, the sizes of particle images vary between 2-6 pixel depending on the camera view (see **Table 2**). An additional correction of global image shifts is subject of ongoing efforts.

Table 3: Residuals of world-to-image mapping in [pixel] and image-to-world mapping in [µm] after least squares minimization of the re-projection error

	Camera 1		*Camera 2*		*Camera 3*		*Camera 4*	
Mapping function	*[px]*	*[µm]*	*[px]*	*[µm]*	*[px]*	*[µm]*	*[px]*	*[µm]*
Pinhole w/o. distorsions	0.30	-	0.33	-	0.24	-	0.27	-
Ratios of 2nd order poly.	0.22	4.7	0.24	6.6	0.17	3.4	0.24	3.9
3rd order polynomial	0.22	4.6	0.24	5.9	0.16	3.1	0.23	3.9

Particle volume reconstruction

Three-dimensional reconstruction of the imaged particle volume is achieved with the maximum entropy reconstruction technique (MENT, [Minerbo, 1979]). MENT was chosen because it offers a number of advantages with respect to the more established methods such as MART [Elsinga et al., 2006] or MLOS-SMART [Atkinson & Soria, 2009]. Foremost MENT can significantly increase reconstruction speed [Bilsky et al., 2012] because the computational complexity is low. In a first approach the particle volume was reconstructed in two MENT iterations at a sampling ratio of approximately 1 voxel per pixel. The reconstruction of two time-steps of a volume of 1800×1200×300 voxel took in the order of 3.8 minutes on a 12-core Intel Xeon workstation at 2.40 GHz and 12 GB RAM. **Fig. 7** shows the obtained particle intensity versus z averaged over 20 realizations and cumulated along volume slices. The ghost intensity background level increases by a factor of two at the thick sheet configuration. This is still subject of further investigation and might be improved by a suitable adaption of image preprocessing, the correction of global image shifts between cameras and by refinement of mapping functions and particle image sampling as described in [Schanz et al., 2012].

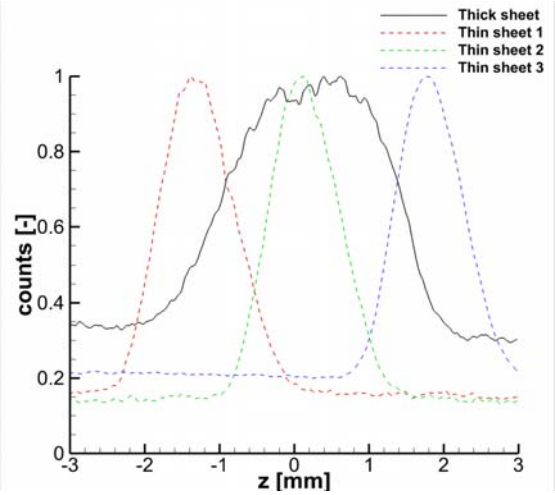

Fig. 7: Reconstructed intensities per volume slice vs. volume depth after MENT reconstruction of the thin sheet and thick sheet volumes within one calibrated region

Particle displacement recovery

State-of-the-art cross-correlation processing is used for particle displacement recovery in both planar and volume PIV. Both algorithms employ a resolution pyramid the starts at a rather coarse grid and stepwise increases resolution while continually updating a predictor field [Scarano, 2002; Raffel et al., 2007]. To increase processing speed, factor N image or volume down-sampling is applied by summing N^2 adjacent pixels or N^3 voxels, respectively. At a given resolution level integer-based sample offsetting is applied in a symmetric fashion using the estimate from the previous resolution step [Westerweel et al., 1997; Wereley et al., 2001]. Intermediate validation is based on normalized median filtering as proposed by Westerweel & Scarano (2005). Once the desired final spatial resolution is reached image or volume deformation based on third-order B-splines [Thévenaz et al., 2000] is applied at least twice to further improve the match between the images or volumes and thereby improving the displacement estimates. The processing codes are highly parallelized using OpenMP [OpenMP] to achieve optimal data throughput.

Stereo PIV measurements

Stereo PIV measurement data is acquired from a thin light sheet setup using cameras no.1 and no.3 with a combined viewing angle of 50°.The image data was processed with PIVview 3.5 (PIVTEC GmbH, Germany). **Fig. 8** shows the secondary flow velocities obtained by averaging $N = 510$ individual PIV recordings. In order to emphasize the chord-wise vortex evolvement, six orthogonal planes are extracted from nine stereo PIV planes. The color represents the *v*-*w*-magnitude while the vectors show the v and w components. Secondary flow velocities in-between the SPIV planes are obtained by inverse distance interpolation. Due to interaction with the main flow the vortex is deformed and velocities in the vicinity of the end wall are clearly increased. The separation region on the blades suction side (see **Fig. 1**) causes an increase of secondary flow velocities near the blades suction side.

Tomo PIV measurements

Fig. 9 shows time-averaged velocities at two neighboring thick sheet positions and boundaries of each reconstructed domain. Six secondary flow planes within the volume are plotted to show the vortex evolvement. The colored contour represents *v*-*w*-magnitude, that is, the in-plane velocity. Regions outside the common intersection of all cameras are blanked as well as regions which have light sheet intensity clearly below 50%. Within each plane only the in-plane components of every third vector are plotted to enhance the visibility of the sec-

ondary flow which otherwise would be lost in the presence of the strong out-of-plane component (mean flow). The passage vortex can clearly be identified. The *v*-*w*-magnitudes are comparable to stereo PIV results (**see Fig. 8,** right). The increased secondary flow velocities near the blades suction side can also be observed in stereo PIV results. The magnitudes in this region are lower due to strong background intensity near the blade surface observed by obliquely viewing cameras no.1 and no.2.

Conclusions

The investigation presented herein demonstrates the applicability of thick sheet tomographic PIV in a highly loaded compressor cascade at Ma_1=0.60. With four simultaneous camera views it was possible to measure the complex corner flow of the cascade volume at three regions with respect to the side wall. The final vector resolution is 54×74×13 vectors at a spacing of 0.64 mm in *x* (chord-wise direction) and a spacing of 0.32 mm in *y* and *z*. Averaged results of the corner flow are presented to show conformance to the expected flow and are comparable to stereo PIV (SPIV) measurements at distinct planes. Improvements of image preprocessing and the correction of global image shifts due to tunnel vibrations can further increase accordance to stereo PIV results. The application of volume resolving thick-sheet PIV (or tomo-PIV) near the trailing edge of the cascade's blades demonstrates the technique's potential of instantaneously resolving secondary flow structures within the separation region of the cascade and its ability to derive three dimensional statistical data of fluctuations of velocity in the turbulent flow region.

Acknowledgments

Funding is provided in part by the EU-project AFDAR (Advanced Flow Diagnostics for Aeronautical Research, project no. 265695) of the 7th Framework Program whose support is gratefully acknowledged. The authors would like to thank Alexander Hergt and Sebastian Grund for their patience and support in operating the transonic cascade facility.

References

Atkinson C, Soria J (2009) An efficient simultaneous reconstruction technique for tomographic particle image velocimetry, *Exp. Fluids* **47**:563-578

Bilsky AV, Markovich DM, Tokarev MP, Lozhkin VA (2012) Low computation cost reconstruction technique for tomo-PIV; *Proceedings: 16th Intl. Symp. on Applications of Laser Techniques to Fluid Mechanics, Lisbon, July*

Elsinga GE, Scarano F, Wieneke B, van Oudheusden BW (2006) Tomographic particle image velocimetry, *Exp. Fluids* **41**(6):933-947, doi 10.1007/s00348-006-0212-z

Hergt A, Steinert W, Grund S (2013) Design and Experimental Investigation of a Compressor Cascade for Low Reynolds Number Conditions, In*:* 21th International Symposium on Air Breathing Engines, ISABE-2013-1104, Busan, South Korea, 09-13 Sept.

Klinner J, Hergt A, Beversdorff M, Willert C (2012) Visualization and piv measurements of the transonic flow around the leading edge of an eroded fan airfoil*;* In*:* 16th Intl. Symp. on Applications of Laser Techniques to Fluid Mechanics, Lisbon, July

Klinner J, Willert C (2012) Tomographic shadowgraphy for three-dimensional reconstruction of instantaneous spray distributions; *Exp. Fluids* **53**:531-543

Minerbo G (1979) MENT: A maximum entropy algorithm for reconstructing a source from projection data. *Graphics and Image Processing* **10**, 1979

OpenMP Application Program Interface, Version 3.1, July 2011, http://www.openmp.org/mp-documents/OpenMP3.1.pdf

Prasad AK (2000): Stereoscopic particle image velocimetry. *Exp. Fluids* **29**(2): 103-116, doi 10.1007/s003480000143

Raffel M, Willert C, Wereley S, Kompenhans J (2007): “Particle Image Velocimetry, A Practical Guide”. Springer Berlin-Heidelberg, ISBN 978-3540723073

Scarano F (2002) Iterative image deformation methods in PIV. *Meas. Sci. Technol.* **13**(1), R1

Schanz D, Gesemann S, Schroeder A, Wieneke B, Novara M (2012) Non-uniform optical transfer functions in particle imaging: calibration and application to tomographic reconstruction, *Meas. Sci. Technol.* (Submitted)

Thévenaz P, Blu T, Unser M (2000) Interpolation revisited. *IEEE Transactions on Medical Imaging* **19**(7):739–758

Wereley ST, Meinhart, CD (2001) Second-order accurate particle image velocimetry. *Exp. Fluids* **31**(3):258–268

Westerweel J, Dabiri D, Gharib M (1997) The effect of a discrete window offset on the accuracy of cross-correlation analysis of digital piv recordings. *Exp. Fluids* **23**(1):20-28

Westerweel J, Scarano F (2005) Universal outlier detection for PIV data. *Exp. Fluids* **39**(6):1096–1100

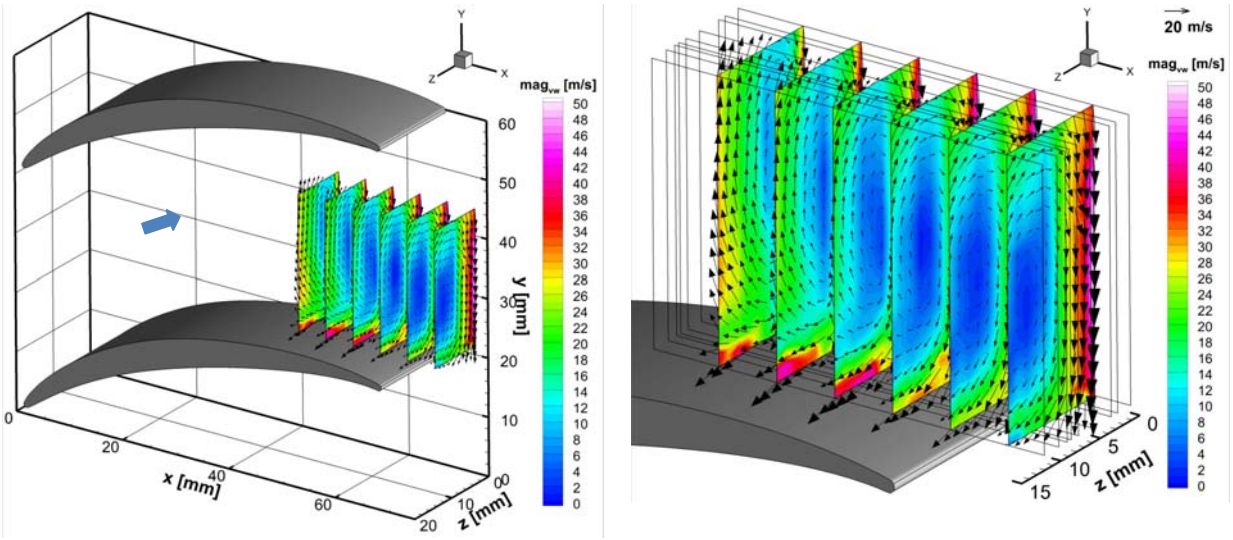

Fig. 8: Secondary flow velocities obtained from averaged SPIV at 9 planes each with 1 mm sheet thickness; overview (left), detailed flow field and boundaries of the SPIV planes (right)

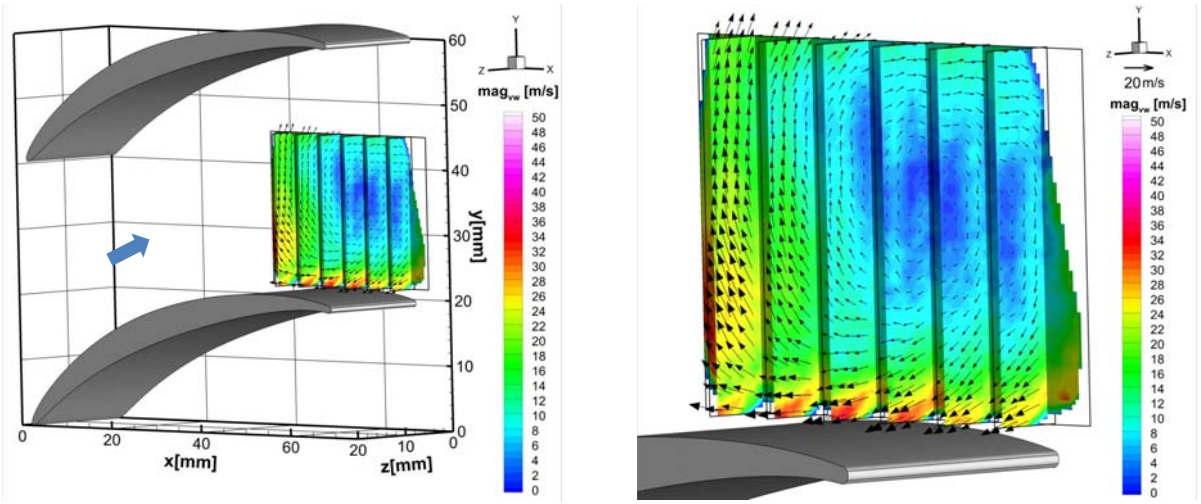

Fig. 9: Average of N=100 tomographic measurements for a volume of 36×24×4 mm³ at z=8 mm distance to the end wall; overview (left) and detailed flow field with boundaries of reconstructed domain (right). Only every third vector along each dimension is plotted